

ABSTRACT

9 A negative shortwave cloud feedback associated with higher extratropical liquid water content in
10 mixed-phase clouds is a common feature of global warming simulations, and multiple mechanisms
11 have been hypothesized. A set of process-level experiments performed with an idealized global
12 climate model (a dynamical core with passive water and cloud tracers and full Rotstaysn-Klein
13 single-moment microphysics) show that the common picture of the liquid water path (LWP)
14 feedback in mixed-phase clouds being controlled by the amount of ice susceptible to phase change
15 is not robust. Dynamic condensate processes—rather than static phase partitioning—directly
16 change with warming, with varied impacts on liquid and ice amounts. Here, three principal
17 mechanisms are responsible for the LWP response, namely higher adiabatic cloud water content,
18 weaker liquid-to-ice conversion through the Bergeron-Findeisen process, and faster melting of ice
19 and snow to rain. Only melting is accompanied by a substantial loss of ice, while the adiabatic cloud
20 water content increase gives rise to a net increase in ice water path (IWP) such that total cloud water
21 also increases without an accompanying decrease in precipitation efficiency. Perturbed parameter
22 experiments with a wide range of climatological LWP and IWP demonstrate a strong dependence
23 of the LWP feedback on the climatological LWP and independence from the climatological IWP
24 and supercooled liquid fraction. This idealized setup allows for a clean isolation of mechanisms
25 and paints a more nuanced picture of the extratropical mixed-phase cloud water feedback than
26 simple phase change.

27 **1. Introduction**

28 With atmospheric warming from greenhouse gases, cloud properties would vary in manifold
29 ways, resulting in further changes in radiative fluxes and climate. Despite the recent advances
30 in mechanistic understanding, the so-called cloud feedback is widely considered to be the largest
31 contributor to the uncertainties in climate sensitivity and model projection of future warming
32 (Sherwood et al. 2020). Ceppi et al. (2017) identifies three robust components of cloud feedback
33 in comprehensive global climate models (GCMs): a positive longwave feedback from rising free
34 tropospheric clouds, a positive shortwave (SW) feedback from decreasing subtropical low cloud
35 fraction, and a negative SW feedback from increasing extratropical cloud optical depth.

36 Uncertainty associated with cloud feedback is dominated by the SW components (Soden and
37 Vecchi 2011; Vial et al. 2013). Among these, this study focuses on the component that affects
38 radiation through altering cloud optical depth or brightness (as opposed to cloud fraction). This
39 cloud optical depth feedback is robustly negative in the Coupled Model Intercomparison Project
40 Phase 5 (CMIP5) GCMs (Zelinka et al. 2016), though it may be artificially tuned to a small range
41 (McCoy et al. 2016), and mechanistic uncertainty still abounds (Gettelman and Sherwood 2016;
42 Ceppi et al. 2017; Korolev et al. 2017). Observations have shown that in pure liquid and mixed-
43 phase (liquid and ice co-existing) clouds, cloud optical depth is primarily controlled by liquid
44 water path (LWP), which is the vertically integrated cloud liquid (Stephens 1978). Ice affects cloud
45 optical depth to a lesser extent owing to larger sizes of ice particles and ice water path (IWP) being
46 generally smaller than LWP (Pruppacher and Klett 2010; McCoy et al. 2014; Cesana and Storelmo
47 2017). GCMs predict a robust extratropical LWP increase in response to global warming, which
48 is thought to be the main driver of the negative SW cloud feedback (e.g. Ceppi et al. 2016).

49 Recent modeling studies have highlighted the need to improve GCM representation of the
50 extratropical cloud feedback. Zelinka et al. (2020) showed that the increased climate sensitivity
51 in CMIP6 models relative to CMIP5 is largely due to changes in this feedback. The multi-model
52 ensemble mean changes from negative in CMIP5 to slightly positive in CMIP6 presumably due to
53 model physics differences. Therefore, it is critical to delineate the underlying mechanisms of the
54 extratropical cloud feedback and its various components.

55 Multiple pathways have been proposed to explain the extratropical increase (Ceppi et al. 2017) in
56 liquid cloud condensate. The first is an increase in the adiabatic cloud water content. With warming,
57 the amount of water condensed in saturated updrafts increases (Tselioudis et al. 1992; Gordon and
58 Klein 2014); the fractional change is greater at colder temperatures (Betts and Harshvardhan 1987;
59 Somerville and Remer 1984). The second mechanism involves phase change in mixed-phase clouds
60 (e.g., Mitchell et al. 1989; Senior and Mitchell 1993; McCoy et al. 2015; Storelvmo et al. 2015; Tan
61 et al. 2018), which occurs only at temperatures below freezing. As isotherms shift upward with
62 warming, the liquid-to-ice ratio at a given mixed-phase cloud location is likely to increase (Tan et al.
63 2016), thereby increasing cloud optical depth. An implication of this phase change mechanism is
64 that since liquid precipitates less efficiently than ice, total cloud water content may increase (Klein
65 et al. 2009; McCoy et al. 2015; Ceppi et al. 2016; McCoy et al. 2018). This work will address
66 both mechanisms and their impacts on LWP and IWP. A third potential mechanism frequently
67 mentioned in the literature is poleward jet shifts. As this effect is highly model dependent and
68 unlikely to be dominant (Kay et al. 2014; Ceppi and Hartmann 2015; Wall and Hartmann 2015;
69 Ceppi et al. 2016), it is not explored here.

70 The relative importance of the proposed mechanisms is still unclear. LWP itself is robustly linked
71 to temperature in both models (Ceppi et al. 2016) and observations (Terai et al. 2019), hinting at the
72 potential for emergent constraints on the negative SW cloud feedback. McCoy et al. (2016) noted

73 that among CMIP5 GCMs, T5050, the diagnosed temperature at which liquid and ice exists in
74 equal amounts globally, is strongly anti-correlated with LWP, but positively correlated with cloud
75 fraction despite the lack of a physical explanation. At the same time, the range of T5050 (as well as
76 a similarly-defined 90% glaciated temperature) estimated from space-borne observations is much
77 lower than that diagnosed from CMIP5 models, suggesting that the models tend to freeze liquid
78 at temperatures that are too high (Cesana et al. 2015; McCoy et al. 2016). Multiple GCM studies
79 (McCoy et al. 2014; Tan et al. 2016; Frey and Kay 2018) have shown that increasing the ratio of
80 supercooled liquid to total water (the so-called supercooled liquid fraction or SLF) in mixed-phase
81 clouds decreases the SW negative feedback, and thus increases climate sensitivity. These results
82 have been attributed to models with higher T5050 having more susceptible ice (McCoy et al. 2018),
83 which is hypothesized to control the feedback strength (as in Tan et al. 2018). Improvements in
84 understanding the governing mechanisms are especially important as some modeling studies with
85 observationally-based constraints have suggested that the negative SW cloud optical depth feedback
86 is too strong or even of the wrong sign in GCMs, implying that the actual climate sensitivity may
87 be underestimated (e.g. Tan et al. 2016; Terai et al. 2016).

88 This work utilizes an idealized model to probe the physical mechanisms underlying the extratrop-
89 ical cloud water feedback. Idealized models complement comprehensive GCMs (Held 2005, 2014)
90 since their workings are relatively easy to understand (Pierrehumbert et al. 2007). This is particu-
91 larly true as previous studies of mixed-phase clouds are hindered by the non-linear complexity of
92 cloud microphysics and the potential for unrealistic interactions between different parameterized
93 processes (Ceppi et al. 2017). We seek to test the plausibility of the leading hypotheses in the
94 mixed-phase cloud feedback literature including the simple conceptual picture of liquid replacing
95 ice with warming, which has fueled the notion of the extratropical LWP feedback being controlled
96 by the amount of susceptible ice. As mentioned above, more ice in the control climate is thought

97 to cause a greater increase in liquid with warming. The main supporting evidence is the positive
98 correlation between the LWP feedback and climatological SLF or T5050 (McCoy et al. 2018; Tan
99 et al. 2018). With a set of targeted, process-level experiments, we seek to explore the complexity
100 of the mixed-phase cloud feedback. We also use a perturbed parameter ensemble of experiments
101 with varied cloud physics settings to investigate the feasibility of predicting the LWP feedback
102 from the control climate.

103 This paper is arranged as follows. Section 2 outlines the methodology. Section 3 presents the
104 results from process-level and perturbed parameter experiments. Section 4 compares with previous
105 studies with the goal of examining the plausibility of the phase change mechanism and other related
106 arguments. Section 5 concludes as to rethinking the physical picture of the extratropical mixed-
107 phase cloud feedback and suggests a path for future research.

108 **2. Methodology**

109 The idealized GCM used here combines a simple dry GCM with passive water and clouds as
110 described in detail in Ming and Held (2018). The core is Held-Suarez dry dynamics (Held and
111 Suarez 1994) at a T42 horizontal resolution (about 2.8° spacing) with 20 equally spaced vertical
112 layers. Passive water vapor and cloud tracers (specific humidity, cloud liquid mixing ratio, cloud
113 ice mixing ratio, and cloud fraction) are included, but are not allowed to feedback on the dynamics
114 (i.e., no latent heating or cloud radiative effects). The cloud tracers evolve following a prognostic
115 large-scale cloud scheme with bulk single-moment microphysics. The sub-grid-scale total-water-
116 based relative humidity (RH) is assumed to follow a beta distribution, which is a function of the
117 grid-mean RH. The beta distribution is designed such that a grid box with a mean total-water-based
118 RH value above a certain threshold value (RH_c , 83.3% at the default half-width of 0.2) would
119 have sub-grid-scale RH over 100%, thus producing clouds. The role of surface evaporation to

120 create the water vapor tracer is mimicked by nudging air parcels below 850 hPa toward saturation
121 as in Galewsky et al. (2005). As clouds are completely decoupled from dynamics, this model is
122 a unique tool for isolating individual mechanisms in a clean fashion without circular feedbacks.
123 With no convective parameterization, the application of the cloud scheme is limited to stratiform
124 clouds (and not any mixed-phase clouds formed in shallow convection). Yet, as noted in Ming
125 and Held (2018), while idealized, this model provides strong representation of cloud distribution
126 in the extratropical free troposphere. The control simulation (Ctrl) is the model's default climate.
127 For Ctrl and all perturbation experiments, the atmospheric state (e.g., temperature and winds) is
128 identical at every time step. All model simulations include a 300-day spin-up, and the next 1000
129 days are averaged for analysis.

130 The bulk microphysics scheme has separate but interconnected treatments of liquid and ice based
131 on Rotstajn (1997) and Rotstajn et al. (2000). The same scheme is also used in the GFDL AM2.1
132 model, one of the two models compared in Ceppi et al. (2016). As shown in Fig. 1, water vapor forms
133 cloud liquid and ice through condensation and deposition, respectively. The initial partitioning of
134 cloud liquid and ice is based entirely on temperature. All condensate at temperatures greater than
135 -40°C is formed as liquid based on the consideration that ice nuclei are generally limited in the
136 atmosphere (Rotstajn et al. 2000). Supercooled liquid (existing between 0° and -40°C) can then be
137 converted to ice principally through the Bergeron-Findeisen (BF) process (and without an explicit
138 treatment of heterogeneous ice nucleation). In the control climate, the primary sink of water vapor
139 (98.8% globally) is conversion to cloud liquid. Microphysical sources of water vapor come from
140 cloud liquid (evaporation), cloud ice (ice sublimation), rain (rain evaporation), and snow (snow
141 sublimation). Together, rain evaporation and snow sublimation, the most significant microphysical
142 sources, comprise 22.3% of all water vapor sources. Surface evaporation (a non-microphysical
143 source) constitutes the main supplier of water vapor (76.4%).

144 Cloud liquid forms rain through autoconversion and accretion. To facilitate conversion of cloud
145 liquid to ice through the BF process, a minimum amount of ice crystal mass (10^{-12} kg) on which
146 deposition can occur is assumed to be always present. (Note that the BF process is not formulated
147 to be explicitly linked to aerosols.) Cloud liquid is also converted to cloud ice through riming
148 (accretion of cloud liquid by ice) and homogeneous freezing (colder than -40°C). Overall, 68.2% of
149 cloud liquid sinks are to rain and 30.9% to cloud ice. Cloud ice is lost almost completely (98.3%)
150 to snow through ice settling. In the microphysics scheme, cloud ice and snow are treated effectively
151 as one species, experiencing the same fall rate, and are only distinguished by their location in or
152 outside of a cloud. Ice and snow can melt into rain: if this takes place in a cloud, it is considered
153 melting of ice; if it takes places outside of a cloud, it is considered melting of snow. Cloud ice is
154 also lost to water vapor through sublimation.

155 The *process-level experiments* involve increasing the temperature field fed to certain parts of
156 the microphysics scheme or the formulation of surface evaporation by 2 K (summarized in Table
157 1). These isolated warming experiments are designed after Ceppi et al. (2016). Here, in the
158 microphysics scheme (same as that used in the AM2.1 aquaplanet in Ceppi et al. (2016)), there
159 are at least four explicitly temperature-dependent processes: partitioning of newly formed cloud
160 condensate, the BF process, homogeneous freezing, and melting of ice and snow. When water
161 vapor experiences condensation/sublimation at the beginning of the microphysics scheme, it is
162 initially partitioned into cloud liquid and ice based solely on temperature. Only liquid is created at
163 temperatures warmer than -40°C , and only ice otherwise. Supercooled liquid can be converted to
164 ice through the BF process, homogeneous freezing, and riming. For the BF process, temperature
165 affects whether or not the process occurs (below 0°C) as well as the rate of cloud liquid being
166 converted to cloud ice, which is greater at lower temperatures (see Eqn. A8). These two effects are
167 tested in combination (BF2K, subjecting the *BF* process to a 2-K warming). (By contrast, riming

168 is not directly dependent on temperature; see Eqn. A10.) Homogeneous freezing of cloud liquid to
169 ice occurs only when the temperature is less than -40°C and converts all cloud liquid to ice. Ice and
170 snow melt into rain only when the temperature is higher than 0°C , with the melting being limited
171 to the amount that would restore the grid-box temperature to 0°C . Melting of ice and snow are
172 tested in combination (ME2K, subjecting *melting* to a 2-K warming). All of these microphysical
173 processes—initial partitioning, the BF process, homogeneous freezing, and melting—are also
174 perturbed in tandem in MI2K (2-K warming of *microphysics*).

175 A significant influence of temperature in the cloud scheme is in the calculation of the saturation
176 specific humidity (q_s) and related variables (the T derivative of q_s , the psychrometric constant,
177 and the sum of the vapor diffusion and thermal conductivity factors) that are used in many parts
178 of the scheme. Since surface evaporation is also formulated in parallel based on q_s , q_s for
179 microphysics and surface evaporation are perturbed simultaneously in Qse2K (2-K warming of q_s
180 for the stratiform cloud scheme and *evaporation*). This experiment enables us to study the effect
181 of the adiabatic cloud water content increase. Finally, to cover all the aforementioned effects of
182 temperature as well as any other effects (such as the influence of temperature on air density), a 2-K
183 temperature increase is fed to the cloud scheme and surface evaporation to create the Tse2K (full
184 warming) experiment.

185 To develop a predictive theory of the extratropical mixed-phase cloud feedback that is applicable
186 to a wide range of control states, a set of *perturbed parameter experiments* (also summarized in
187 Table 1) are created by systematically modifying three key parameters of the cloud scheme. The
188 first two have been suggested as significant for the mixed-phase cloud feedback: the strength of
189 the BF process may be too efficient (Tan et al. 2016) and RH_c too high (McCoy et al. 2016). To
190 vary the strength of the BF process, the formula for the conversion rate is altered arbitrarily by
191 multiplying with a constant (0.25, 0.5, 2 or 4). The corresponding experiments are labeled as

192 quarBF, halvBF, doubBF and quadBF. Note that these adjustments do not result in actual changes
 193 in the BF rate as large as those imposed. The effective RH_c (83.3% in Ctrl) is varied from 76.7% to
 194 90.0% at increments of $\sim 3.3\%$ (rh767, rh800, rh867, and rh900) by altering the half-width of the
 195 sub-grid-scale RH beta distribution. Finally, a third parameter is chosen to cleanly affect the mean-
 196 state amount of cloud ice: the fall speed of cloud ice (relative to the large-scale vertical motion) is
 197 perturbed by multiplying with a constant (0.5, 0.75, 1.25 or 1.5). The corresponding experiments
 198 are v050, v075, v125 and v150. For each of these states, a Tse2K simulation (increasing the
 199 temperature field fed to the cloud scheme and surface evaporation by 2 K) is created, and the
 200 response (for example, rh767_Tse2K minus rh767) analyzed.

201 The key to understanding the steady-state mixing ratios of cloud liquid and ice (q_l and q_i ,
 202 respectively) and their responses to the warming is how they are related to the time tendencies of
 203 the aforementioned microphysical processes. To illustrate the point, let us write the time derivative
 204 of a variable q (q_l or q_i) as:

$$\frac{dq}{dt} = s - aq^b, \quad (1)$$

205 where s is the source term, and the sink term is parameterized as a power-law function of q with a
 206 and b as constants. It follows that the fractional change of q can be related to the fractional change
 207 of s by:

$$\frac{\delta q}{q} = \frac{1}{b} \frac{\delta s}{s}. \quad (2)$$

208 The formulation and behavior of the autoconversion parameterization (Eqn. A1) are discussed
 209 in Golaz et al. (2011) (see their Equations 12-14). Although the rate is nominally proportional
 210 to $q_l^{7/3}$, it is effectively controlled by a numerical limiter (Eqn. A3), which tends to set q_l at a
 211 critical value (q_{crit}) determined by a tunable threshold droplet radius (r_{thresh}) and droplet number
 212 concentrations (N). Since neither r_{thresh} nor N changes in this study, q_l should be close to q_{crit}

213 when autoconversion is the dominant process. By contrast, accretion is proportional to q_l and the
214 flux of rain (Eqn. A4). The BF rate (Eqn. A8) is effectively independent of q_l , but conditionally
215 proportional to $q_i^{1/3}$. Riming (Eqn. A10) is proportional to q_l and the flux of settling ice, which is
216 related to the fall speed and q_i . Similarly, ice settling (Eqn. A6) at a specific level is determined
217 by the fall speed and vertical gradient of q_i ($\partial q_i / \partial p$, where p denotes pressure). If q_i is altered by
218 the same ratio throughout the column, an assumption that holds approximately for the simulations
219 examined here, the fractional change in the ice settling rate would be the same as that in q_i . The
220 microphysical tendency equations are listed in the Appendix for reference. Condensation and
221 deposition, the main sources of cloud liquid and ice, are not directly related to q_l or q_i .

222 The analysis focuses on two variables: LWP and IWP, which are, respectively, vertically inte-
223 grated cloud liquid and cloud ice in units of g m^{-2} . Absolute and fractional changes in LWP and
224 IWP are normalized by warming and thus given in units of $\text{g m}^{-2} \text{K}^{-1}$ and $\%$ K^{-1} , respectively.
225 Due to the highly simplified nature of the boundary layer in this model (i.e., surface evaporation
226 saturating the air below 850 hPa), for the purposes of this analysis the vertical integral has a lower
227 boundary of 850 hPa such that LWP and IWP only represent the cloud condensate above 850 hPa.
228 Similarly, specific humidity and cloud condensate tendency terms, when column-integrated, only
229 represent values above 850 hPa. 30° to 60° and 60° to 90° are considered the mid-latitudes and
230 high-latitudes, respectively, and together they are considered the extratropics. Data is averaged
231 between the two hemispheres because of the hemispheric symmetry of the simulated climate. The
232 supercooled liquid fraction (SLF) is calculated as the ratio of cloud liquid to total cloud water
233 (liquid and ice). The daily SLF is binned as a function of temperature at an interval of 0.1 K
234 for each grid box in the extratropical region above 850 hPa with the temperature at which SLF is
235 closest to 50% considered to be T5050 (liquid and ice partitioned equally).

236 3. Results

237 a. Process-level Experiments

238 Fig. 2 shows the zonal-mean LWP and IWP (averaged between hemispheres) in the control
239 case (Ctrl), yielding a picture of the model's default climate [see Ming and Held (2018) for other
240 related variables including RH and CF]. Here, LWP dominates IWP equatorward of the storm
241 tracks (at around 45°); note that this LWP/IWP ratio is not directly comparable with full GCMs
242 as here the boundary layer is excluded in the calculation of LWP and IWP. In the total warming
243 experiment (Tse2K), the general features, including the location of the storm tracks, remain the
244 same. Both LWP and IWP are higher at all latitudes in the warmer climate. The increase in LWP
245 is more pronounced than that in IWP in the mid-latitudes, while they are more comparable in the
246 high-latitudes.

247 Table 2 and Fig. 3 break down the LWP and IWP feedbacks seen in Tse2K. The increase in
248 LWP (Fig. 3a) in the extratropics is dominated by the microphysical component (MI2K) with a
249 much smaller (slightly less than 20%) contribution from the increased q_s (Qse2K). MI2K and
250 Qse2K combine nearly linearly to produce the full Tse2K increase in LWP suggesting that Tse2K
251 does not add any significant temperature-affected processes beyond those perturbed in MI2K and
252 Qse2K. The LWP feedback from the adiabatic water content increase is stronger in the high-
253 latitudes ($5.2\% \text{ K}^{-1}$) than in the mid-latitudes ($1.6\% \text{ K}^{-1}$), as one would expect from the nonlinear
254 temperature-dependence of the Clausius-Clapeyron relation.

255 Within the combined microphysical component, the BF process (BF2K) is responsible for most
256 of the LWP increase, with a smaller contribution from melting (ME2K) present only in the mid-
257 latitudes (Fig. 3b), and homogeneous freezing and initial phase partitioning producing negligible
258 results (presumably because of the small amount of cloud condensate present near -40°C). The

259 BF effect is realized through the temperature-dependence of the conversion rate, as opposed to the
260 temperature threshold at which the BF process takes control. LWP increases as the BF process
261 slows down, converting less liquid to ice. The melting of snow to rain dominates the melting of ice
262 to rain in terms of their effects in enhancing LWP. As discussed later, this can be conceptualized as
263 a consequence of weaker riming since there is less snow (falling ice) to collect cloud liquid. Thus,
264 we conclude that the increase in LWP with warming results primarily from a significant weakening
265 of the BF process.

266 The IWP feedback is more nuanced. As shown in Fig. 3c, Qse2K and MI2K produce opposite
267 effects: IWP increases at all latitudes in the former, while it decreases in the mid-latitudes with no
268 significant change in the high-latitudes in the latter. In Qse2K, the normalized fractional increase
269 in the high-latitude IWP ($7.9\% \text{ K}^{-1}$) is greater than the mid-latitude counterpart ($6.7\% \text{ K}^{-1}$),
270 consistent with the adiabatic water content increasing with temperature at a faster rate at colder
271 temperatures. The net result in Tse2K, to which Qse2K and MI2K add effectively linearly, is an
272 increase in IWP, principally poleward of 45° . The relative importance of the BF process versus
273 melting is reverse to the LWP feedback. The microphysical effect is dominated by ME2K (Fig. 3d);
274 the enhanced melting of snow contributes to the lowering of IWP more than that of cloud ice. By
275 contrast, BF2K gives rise to very little change in IWP. The fact that a weakening of the BF process
276 causes a large increase in LWP, but no concurrent decrease in IWP is somewhat counter-intuitive,
277 a point to which we will return later in this section when discussing the BF2K results in detail. (As
278 with LWP, perturbing homogeneous freezing or initial phase partitioning produces no significant
279 change in IWP.)

280 Fig. 4 shows the vertical structures of the changes in the mixing ratios of cloud liquid and ice.
281 To better understand the underlying physical mechanisms, the main tendency terms driving the
282 steady-state cloud liquid and ice are plotted in Figs. 5 and 6, respectively. No appreciable change

283 in q_l is present below the freezing line in any experiment (Fig. 4) even when there are large local
284 changes in cloud liquid tendencies, as is the case for condensation in Qse2K (Fig. 5a). It is also
285 clear from Fig. 5 that autoconversion and accretion are the principal sinks of q_l above 0°C in
286 Ctrl, with autoconversion slightly stronger. As explained in Section 2, q_{crit} exerts a strong control
287 over q_l when autoconversion dominates. By contrast, the BF process and riming take over in the
288 mixed-phase cloud temperature range (between 0° and -40°C). Both the BF process and riming
289 increase with the enhanced condensation in Qse2K (Fig. 5m and q). While the BF process is
290 independent of q_l , since riming is proportional to q_l steady-state q_l increases (Fig. 4a). On the ice
291 side, faster riming acts to increase q_i (Fig. 6e). Moreover, the increased condensation leads directly
292 to higher q_i through the BF process (Fig. 6a), which is conditionally proportional to $q_i^{1/3}$. The
293 resulting higher flux of settling ice, which is formulated to be approximately proportional to q_i ,
294 tends to further accelerate riming, but lower q_l . This cancels out much of the increase in q_l caused
295 by the increased condensation (Fig. 4a). The end result is that the normalized fractional increase
296 in the extratropical IWP ($6.8\% \text{ K}^{-1}$) is much greater than the LWP counterpart ($1.7\% \text{ K}^{-1}$).

297 The imposed warming to the BF process (BF2K) slows down the BF conversion from liquid
298 to ice (Fig. 5n). Since autoconversion and accretion play limited roles in the mixed-phase cloud
299 regime, an acceleration of riming (Fig. 5r) is the only way to re-establish the q_l tendency balance,
300 causing a significant increase in q_l (Fig. 4b). This re-balancing can be conceptualized as a weaker
301 BF process producing more cloud liquid to be scavenged by falling ice through riming. Since
302 the q_l and q_i tendencies (and their changes) are of the same magnitude but opposite signs for the
303 BF process and riming, the effect of the two processes on q_i is dictated by the balance of their
304 q_l counterparts (Fig. 6b and f). Because the effects of q_i are of opposing sign, there is near-zero
305 net change in cloud ice (Fig. 4f). This somewhat counterintuitive result emphasizes the need to
306 evaluate changes in q_l and q_i based on process changes and a dynamic re-balancing of sources

307 and sinks. For example, when weakened BF process (as through warming) experiments were run
308 with the riming process entirely removed from the microphysics scheme, instead of BF process q_i
309 tendency change being balanced principally by enhanced riming with little change in ice settling
310 (as shown in Fig. 6f and j), without riming, the tendency change was principally balanced by
311 significantly weakened ice settling.

312 The melting perturbation (ME2K) is unique in the sense that the resulting changes in cloud liquid
313 and ice are of mirror image in terms of spatial structure (Fig. 4c and g). The main reason is that the
314 melting perturbation effects are relatively confined to a narrow domain of a few degrees above the
315 time-averaged freezing line. The warming-induced additional melting acts to increase the flux of
316 rain and decrease the flux of settling ice simultaneously. Both factors have implications for q_l . The
317 former tends to accelerate accretion with an effect of decreasing the q_l tendency, while the latter
318 acts to slow down riming which increases the q_l tendency. The simulation shows a net increase of
319 q_l , suggesting that the latter factor prevails over the former. The signs of the simulated rate changes
320 are consistent with the expectations, and they largely balance out each other (Fig. 5k and s), with
321 a weaker contribution from autoconversion (Fig. 5g). On the ice side, the reduced supply of ice
322 from riming is balanced entirely by lowering q_i and thus settling (Fig. 6g and k). The role of the
323 BF process here is negligible as it is relatively ineffective at temperatures within a few degrees of
324 0 °C.

325 This process-level analysis illustrates why the principal components of the full warming (Tse2K)
326 simulation, namely Qse2K, BF2K, and ME2K, increase q_l and hence LWP, as summarized schemat-
327 ically in Fig. 7. Although they all point in the same direction, the microphysical warming com-
328 ponents (BF2K and ME2K) are a stronger contribution to the LWP feedback than the macro-
329 physical/thermodynamic component (Qse2K). The extratropical IWP feedback stems from a broad
330 increase in q_i from Qse2K being offset partially by a decrease near the freezing line from ME2K.

331 The results underscore that multiple processes with distinct characteristics are influential in shaping
332 the LWP and IWP responses, and contradict the common picture suggested in mixed-phase cloud
333 feedback literature of an effective trade-off between ice and liquid. Here, the dominant processes
334 which increase LWP with warming in mixed-phase clouds are not doing so at the expense of ice,
335 so the actual picture is more complicated than a (direct or indirect) replacement of ice with liquid
336 with warming. Liquid and ice in mixed-phase clouds are not in a static equilibrium; rather, they
337 exist in a dynamic balance of sources and sinks. These source and sink processes are directly
338 changed by warming as opposed to a simple temperature-dependent phase partitioning.

339 *b. Perturbed Parameter Experiments*

340 To further explore the sensitivity of the LWP and IWP feedbacks, a set of alternative control
341 states was created by altering three key aspects of the cloud scheme, namely the value of RH_c ,
342 the strength of the BF process and the fall speed of ice (v_{fall} , Eqn. A7), summarized in Table
343 1. As shown in Fig. 8, the first two changes produce a wide range of the climatological LWP
344 (approximately a factor of 2), but little variation in IWP. Lower RH_c or weaker BF process leads
345 to higher LWP. While these experiments are not designed to fully explain the insensitivity of IWP
346 to RH_c or the BF process in more detail than the previous section, the broad principle is that
347 steady-state values are determined by a dynamic balance of continuing phase conversion, not a
348 static equilibrium. And, ice changes are harder to manufacture using local processes (like the BF
349 process) when ice is so strongly controlled by gravitational settling. In the v_{fall} perturbations,
350 IWP varies widely (a factor of more than 3) with higher fall speed giving rise to lower IWP but
351 with little spread in the climatological LWP.

352 All of these perturbed parameter experiments are subjected to 2-K warming in a way analogous
353 to Tse2K. The resulting normalized LWP and IWP changes (δLWP and δIWP , respectively) are

354 plotted against their climatological counterparts in Fig. 9. Ranging from 2.6 to 3.4 g m⁻² K⁻¹,
355 relative to 3.0 g m⁻² K⁻¹ in Tse2K (Table 2), the LWP feedback is positively correlated with the
356 climatological LWP (Fig. 9a). The best linear fit yields that $\delta\text{LWP} = 0.045 \text{ LWP} + 1.60$, with an R^2
357 of 0.98. Thus, the fractional change can be written as $\delta\text{LWP}/\text{LWP} = 0.045 + 1.60/\text{LWP}$, suggesting
358 that the marginal gain decreases with increasing LWP. Since the four experiments targeting the BF
359 process, namely {quar, halv, doub, quad}BF, effectively demonstrate the basic behavior of the LWP
360 feedback, we start by focusing on them in the effort to explain the latter. As shown above, the main
361 sink terms for cloud liquid in the mixed-phase regime are the BF process and riming. As the BF
362 process becomes stronger from quarBF to quadBF, riming has to weaken if the total sink is constant,
363 giving rise to lower climatological LWP, in line with the model simulations. Recall that the riming
364 rate is proportional to cloud liquid. The process-level experiments suggest that the warming effect
365 is realized mostly through the BF process. In these experiments, the warming-induced perturbation
366 to the BF process is roughly proportional to its baseline rate (not shown). Therefore, the lower
367 the climatological LWP is, the stronger the baseline BF rate and associated perturbation are. The
368 combination translates into higher fractional change in LWP with lower climatological LWP (from
369 a stronger BF process).

370 Lowering RH_c tends to increase LWP by enhancing condensation in a way similar to Qse2K.
371 They differ in that the former causes a large increase in autoconversion, but without any substantial
372 change in accretion or riming, while all three processes increase in the latter. As explained
373 before, autoconversion can adjust to forced changes such as those resulting from warming without
374 perturbing cloud liquid. As a result, a control state with enhanced autoconversion should be less
375 sensitive to warming (in this limited context; other feedbacks in complex models such as that
376 noted in Mülmenstädt et al. (2021) may complicate this picture). This explains why lowering RH_c
377 gives rise to larger LWP, but smaller fractional increases in response to warming. Of interest is

378 the minimal effect on the extratropical climatological LWP and δ LWP from drastically changing
379 the climatological IWP (or susceptible ice) in the ice fall speed experiments. Clearly, the LWP
380 feedback is correlated with the climatological LWP, but not the climatological IWP. The preceding
381 analysis also holds when the LWP feedback is further divided into the mid- and high-latitude
382 components (not shown).

383 The IWP feedback is correlated strongly with the climatological IWP (Fig. 9b). Note that the
384 variation in the IWP feedback is almost exclusively from the ice fall speed experiments (ranging
385 from 0.57 to 1.70 g m⁻² K⁻¹). An inspection of the best linear fit result (δ IWP = 0.023·IWP
386 + 0.031, with an R^2 of 1.00) indicates that the intercept is so small that the warming-induced
387 change in IWP is effectively proportional to the climatological IWP. In other words, the normalized
388 fractional change is constant at 2.3% K⁻¹. This relatively simple relation reflects the fact that
389 gravitational settling is the main process through which cloud ice can be adjusted to re-establish
390 the mass balance. As seen both from the process-level experiments and the BF-series parameter
391 perturbation experiments, the amount of cloud ice is not sensitive to the BF process. In the
392 meantime, riming is under the strong control of the cloud liquid balance. This leaves gravitational
393 settling as the only way to alter cloud ice without affecting other processes substantially. Note
394 that similar linear relationships hold if the climatological LWP and IWP are computed only for the
395 mixed-phase temperature range (between 0 and -40°C), confirming the independence of the LWP
396 feedback from the climatological IWP (or susceptible ice).

397 **4. Discussion**

398 As noted in the introduction, much of the existing literature on the extratropical mixed-phase cloud
399 feedback centers on the correlation between the climatological SLF/T5050 and LWP feedback.
400 Specifically, the lower SLF is or the higher T5050 is, the stronger the LWP feedback is (Tan et al.

2016; Frey and Kay 2018; McCoy et al. 2018). The presumption is that the phase change mechanism plays a crucial role, meaning that ice would be statistically replaced by liquid as isotherms shift with warming. Thus, the climatological susceptible ice or IWP is thought to be predictive of the feedback strength, forming the basis of potential emergent constraints (Tan et al. 2016). A related argument is that the phase change would give rise to a decrease in precipitation efficiency and a net increase in total water path (TWP, the sum of LWP and IWP) as liquid is less efficient than ice in forming precipitation (McCoy et al. 2018). While it is clear from the previous section that the mixed-phase cloud feedback is much more complicated than simple phase change, we further test the validity of both claims—SLF/T5050 as a predictor and decreased precipitation efficiency increasing TWP—against our results.

The range of climatological T5050 in the perturbed parameter experiments is shown in Fig. 10: stronger BF process and higher RH_c favor lower LWP (or SLF) and higher T5050. The normalized δLWP , however, is strongly anti-correlated with T5050 ($R^2 = 0.92$, Fig. 10) as it is positively correlated with the climatological LWP (Fig. 9a). The T5050/ δLWP anti-correlation is opposite to that expected if susceptible ice drove the LWP feedback and is contrary to the findings of Tan et al. (2016) and Frey and Kay (2018) based on the CAM5 model and of McCoy et al. (2018) based on CMIP5 models. Furthermore, as shown in Fig. 8, the climatological IWP is effectively constant for these experiments. This calls into question the hypothesis that susceptible ice controls the strength of the LWP feedback. As another evidence against the hypothesis, if the v_{fall} perturbations are included, the predictive power of T5050 is significantly diminished ($R^2 = 0.76$, Fig. 10). The large variations in the climatological IWP, which drive the spread in T5050 in the v_{fall} perturbations, do not affect δLWP significantly. Thus, any connection here between T5050 and the LWP feedback is not derived from the climatological ice but rather the climatological liquid. This finding suggests that it is important to, when showing correlation between changes in T5050 (or SLF) and LWP

425 feedback or climate sensitivity, also consider the independent roles of changes in climatological
426 liquid or ice as potentially meaningful in addition to their ratio.

427 To understand why a T5050/LWP feedback connection might be present in some models but
428 not others, we consider the dissection of mechanisms for LWP increase in aquaplanet versions
429 of CAM5 and AM2.1 in Ceppi et al. (2016). AM2.1 uses virtually the same large-scale cloud
430 parameterizations as our idealized model, and the AM2.1 results documented in Ceppi et al.
431 (2016) are in excellent agreement with ours despite numerous differences in model setup and
432 experimental design, a testament to the central role of cloud parameterizations in determining the
433 feedback. Whereas both CAM5 and AM2.1 yield higher LWP in response to warming, their IWP
434 changes differ in sign (see their Figure 2). IWP decreases in CAM5, but increases in AM2.1.
435 Moreover, microphysical processes, especially the BF process, are responsible for the majority
436 of the LWP increases, but cannot even account for the signs of the combined extratropical IWP
437 changes (their Figure 7): the microphysically-induced IWP change is an increase in CAM5 and a
438 decrease in AM2.1. Note that CAM5 implements the Morrison-Gottelman microphysics scheme
439 (Morrison and Gottelman 2008), which differs significantly from the Rotstayn-Klein microphysics
440 scheme (Rotstayn 1997) used in AM2.1 and our model, particularly in the treatment of ice and
441 snow. As noted previously, the Rotstayn-Klein scheme treats cloud ice and snow indistinguishably
442 and therefore lacks direct representation of cloud ice autoconversion and accretion by snow (though
443 tuning of the ice fall speed can indirectly account for these sinks of cloud ice). Additionally, the
444 Morrison-Gottelman scheme includes a representation of ice nucleation, which was found in Tan
445 and Storelvmo (2016) to have an even stronger effect than ice fall speed on LWP and IWP. Similarly,
446 by using the BF process to principally partition liquid and ice between 0°C and -40°C, the Rotstayn-
447 Klein scheme does not directly account for increasingly recognized efficient ice nuclei (Kanji et al.
448 2017). In this sense, it is not inconceivable to see microphysically-induced IWP changes being

449 qualitatively different between the two models. Clearly, the large discrepancy in IWP response to
450 warming merits further analysis and evaluation of both microphysics schemes, especially given the
451 important role of ice cloud microphysics for Arctic cloud feedback (Tan and Storelvmo 2019).

452 Beyond the microphysical feedback, in the Ceppi et al. (2016) study, if one assumes linear
453 additivity (which appears to hold) the non-microphysical component of the IWP change would be
454 a net loss in CAM5 and a net gain in AM2.1. Our results demonstrate that the non-microphysical
455 enhancement of IWP in AM2.1 is attributable to the adiabatic cloud water content increase, a
456 possibility noted in Ceppi et al. (2016). Thus, attempting to reconcile this work with others raises
457 the intriguing question of what factors could outweigh the adiabatic cloud water content effect
458 (however strong it is) and cause the net loss seen in CAM5. These factors (perhaps related to
459 convective ice) should be further explored in complex GCMs and the adiabatic ice effect evaluated
460 for robustness. From the process dissection in Ceppi et al. (2016), it appears that the considerable
461 loss of cloud ice in the warming experiments conducted with CAM5 in Tan et al. (2016) and Frey
462 and Kay (2018) is not microphysical (stratiform) in origin, and thus should not be interpreted
463 as being related to the concurrent increase of cloud liquid, which roots in microphysics. This
464 mechanistic understanding casts further doubt on the susceptible ice hypothesis and other related
465 arguments. From a broader perspective, Ceppi et al. (2016) also noted a robust extratropical
466 LWP increase with warming in the CMIP5 model ensemble mean, without a compensating large
467 decrease in IWP. This is consistent with other studies showing diverse extratropical LWP and IWP
468 feedbacks in models beyond the two highlighted by Ceppi et al. (2016). For example, Lohmann
469 and Neubauer (2018), using ECHAM6-HAM2 with microphysics after Lohmann and Roeckner
470 (1996), found no increase in ECS with increased SLF (unlike the relation found in Tan et al. 2016).
471 McCoy et al. (2021) showed that among CMIP5 and CMIP6 GCMs, most show an increase in
472 liquid along with a slight reduction in ice.

473 Having seen no evidence of the utility of SLF/T5050 as a predictor here for LWP feedback, we
474 now consider whether decreased precipitation efficiency contributes here to the increase in TWP.
475 We calculate the large-scale precipitation efficiency as defined in Zhao (2014), which is the ratio
476 of the total cloud condensation rate (the sum of condensation and deposition fluxes) to surface
477 precipitation and represents the fraction of the condensate that subsequently rains out. There is a
478 slight increase in precipitation efficiency with warming (80.5% in Ctrl versus 81.1% in Tse2K).
479 This results from microphysical increases (80.7% in BF2K and 80.8% in ME2K) being offset by a
480 macrophysical decrease (80.0% in Qse2K). All changes are on the order of 1% or less. Critically,
481 no evidence of an increase in cloud lifetime is present, with precipitation efficiency increasing
482 rather than decreasing. Another measure of a precipitation efficiency effect is surface precipitation
483 normalized by TWP (P/TWP) as in McCoy et al. (2015), which can be thought of as the inverse
484 of the cloud water residence time. Following the Clausius-Clapeyron relation, the extratropical
485 surface precipitation increases by 6.9% K^{-1} in Tse2K and Qse2K, but remains essentially constant
486 in the microphysical experiments. P/TWP increases by 1.9% from 1.03 hr^{-1} in Ctrl to 1.05 hr^{-1}
487 in Tse2K. Again, the net result is a slight decrease in the cloud water residence time or a slight
488 increase in precipitation efficiency. These results do not support a precipitation efficiency effect
489 with warming here as widely claimed (e.g., at the heart of the argument of Bjordal et al. 2020).

490 This finding does not mean a precipitation efficiency feedback is not present in reality, but it
491 may not be present in models as assumed. Mülmenstädt et al. (2021) showed that when warm rain
492 parameterizations are adjusted to better simulate reality in a complex GCM (ECHAM-HAMMOZ),
493 a large negative cloud lifetime effect becomes present. Here we show that other mechanisms can
494 explain a significant increase in LWP and TWP, emphasizing the need to carefully diagnose
495 mechanisms to explain model results which may not contain a significant precipitation efficiency
496 feedback without a warm rain efficiency adjustment. In our model, the weakening of the BF process

497 (BF2K) increases TWP while keeping precipitation nearly constant, suggesting that the BF process
498 alone could affect precipitation efficiency, and thus should be the focus of research to improve
499 its representation in models in addition to the need for improvement in warm rain efficiency as
500 highlighted by Mülmenstädt et al. (2021)

501 Here, in the absence of a precipitation efficiency-mediated strong phase change effect, the adia-
502 batic cloud water content effect is shown to be responsible for increasing TWP by enhancing both
503 liquid and ice. McCoy et al. (2015) observed that increasing TWP was a significant contribution
504 to increased extratropical LWP in CMIP5 models, with 20–80% of the LWP increase being due
505 to phase re-partitioning. Using observations and modeling, McCoy et al. (2019) highlighted the
506 primacy of the adiabatic cloud water content effect in explaining the increase in LWP with warm-
507 ing in extratropical cyclones. It was found that more than 80% of the enhanced Southern Ocean
508 extratropical cyclone LWP in GCMs from warming can be predicted based on the relationship
509 between the climatological warm conveyor belt moisture flux and cyclone LWP and the change in
510 moisture flux with warming (see also McCoy et al. 2020). While phase change may play a role in
511 the remaining unexplained LWP increases, especially in the poleward half of cyclones, it is clearly
512 a secondary mechanism. A ground-based observational study (Terai et al. 2019) found that both the
513 moist adiabatic scaling and phase partitioning mechanisms are equally important for explaining the
514 increase in LWP with warming at cold temperatures. A complementary space-based observational
515 study (Tan et al. 2019), however, suggests phase change is more important than the adiabatic cloud
516 water content increase in explaining the increase in cloud optical depth with cloud top temperature.
517 Between these observational studies, the GCM studies referenced in this Discussion section, and
518 the idealized modeling results presented herein, it is clear that more research is clearly needed
519 for elucidating the relative importance of the two mechanisms. These mechanisms, as well as a

520 potential precipitation efficiency mediated effect, should be carefully diagnosed in future GCM
521 research as an important step in constraining the mixed-phase cloud feedback.

522 **5. Conclusions**

523 This study used an idealized GCM to perform a set of process-level experiments which delin-
524 eated three key mechanisms of the extratropical LWP feedback involving mixed-phase clouds:
525 higher adiabatic cloud water content, weaker liquid-to-ice conversion through the BF process, and
526 strengthened melting of ice and snow to rain with associated impacts on riming. Over half of
527 the extratropical LWP increase can be attributed to the weakening of the BF process, without a
528 corresponding decrease in IWP. The extratropical IWP in fact increases with warming due to the
529 adiabatic cloud water effect, with a small offset caused by stronger melting. Warming experiments
530 in a perturbed parameter ensemble demonstrate a strong dependence of the LWP feedback on the
531 climatological LWP and independence from the climatological IWP. T5050 is anti-correlated with
532 δ LWP and is therefore only useful as a predictor insofar as it represents the climatological LWP as
533 opposed to the climatological IWP. No associated decrease in precipitation efficiency is found in
534 this modelling setup.

535 The overarching goal of this study is to improve mechanistic understanding of the extratropical
536 mixed-phase cloud feedback. Our results help refine the current physical conceptualization of the
537 LWP feedback as more nuanced than simple phase change, involving impacts of higher adiabatic
538 cloud water content, weaker cloud liquid sinks such as the BF process, and indirect phase changes
539 moderated by precipitation processes (especially riming). Liquid and ice in mixed-phase clouds
540 are in a dynamic equilibrium with microphysical process efficiencies defining time-averaged phase
541 partitioning and its change with warming. These results are helpful for guiding efforts to constrain
542 mixed-phase parameterizations in GCMs through process-oriented diagnostics. In particular, the

543 effect of warming on the BF process, which is at the heart of mixed-phase cloud microphysics,
544 should be better understood and represented in GCMs (see Tan and Storelvmo 2016). In addition
545 to the BF process, the climatological LWP needs to be better constrained. Not only is it shown here
546 to be predictive of the LWP feedback, but also the radiative impact of increases in LWP is highly
547 dependent on the control state (Bodas-Salcedo et al. 2016, 2019). Finally, similar process-based
548 studies among varying microphysics schemes (including those with more comprehensive treatments
549 of cloud ice and ice nucleation) are vital, as cloud water source and sink efficiencies define the
550 mixed-phase cloud phase partitioning (Ceppi et al. 2016). Mixed-phase cloud studies should show
551 results at the process level to better conclude as to the driving mechanisms and implications for
552 climate sensitivity. Because of complex interactions in full GCMs when mixed-phase physics are
553 perturbed (as in Tan et al. 2016; Frey and Kay 2018), idealized setups such as that utilized here
554 present a clean, complementary approach for elucidating causal relationships.

555 *Acknowledgments.* The authors acknowledge Nadir Jeevanjee, David Paynter, and three anony-
556 mous reviewers for helpful feedback and Daniel McCoy for useful discussion. M.E.F. was supported
557 by award NA18OAR4320123 from the National Oceanic and Atmospheric Administration, U.S.
558 Department of Commerce, and award AWD1005319 from the National Science Foundation.

559 *Data availability statement.* The output from the simulations described in this manuscript is
560 archived at the Geophysical Fluid Dynamics Laboratory and is available upon request.

561 APPENDIX

562 **Microphysical Transformation Equations**

563 The following equations are those parameterized in the microphysical scheme used herein (after
564 Rotstayn 1997; Rotstayn et al. 2000).

565 *a. Precipitation Formation Processes*

566 *Autoconversion*: the time rate change of grid mean liquid from autoconversion is parameterized
567 as:

$$\frac{\partial q_l}{\partial t} \Big|_{au} = -q_a \times \left(\frac{0.104 g \rho^{4/3} E_{c,au}}{\mu (N \rho_l)^{1/3}} \right) \times (q_l/q_a)^{7/3} \times H(r_d - r_d^{au}) \quad (\text{A1})$$

568 where μ is the dynamic viscosity of air, $E_{c,au}$ is the mean collection efficiency of the autoconversion
569 process, ρ_l is the density of pure liquid, and N is the number of cloud droplets per unit volume. In
570 the Heaviside function, H , r_d^{au} is a critical drop radius that the mean volume radius of cloud drops,
571 r_d , must exceed for autoconversion to occur, where:

$$\rho q_l / q_a = 4\pi N \rho_l r_d^3 / 3 \quad (\text{A2})$$

572 Autoconversion is limited to that which would decrease q_l to the threshold:

$$\text{MAX} \left(- \frac{\partial q_l}{\partial t} \Big|_{au} \right) = \ln \left(\frac{\rho q_l / q_a}{4\pi N \rho_l (r_d^{au})^3 / 3} \right) \times \frac{q_l}{\Delta t_{cld}} \quad (\text{A3})$$

573 *Accretion*: the time rate change of grid mean liquid from accretion is parameterized as:

$$\frac{\partial q_l}{\partial t} \Big|_{acc} = -a_{rain}^{cld} \times 65.8 E_{c,acc} (R_{rain}^{cld} / \rho_l a_{rain}^{cld})^{7/9} \times (q_l / q_a) \quad (\text{A4})$$

574 where R_{rain}^{cld} is the grid mean flux of rain entering the rid box from above that enters saturated air,
575 a_{rain}^{cld} is the portion of the grid box that this occurs in, and $E_{c,acc}$ is the collection efficiency between
576 rain drops and cloud droplets which is parameterized as:

$$E_{c,acc} = r_d^2 / (r_d^2 + 20.5 \mu^2) \quad (\text{A5})$$

577 *Gravitational Settling*: the sink of cloud ice due to gravitation settling is:

$$\frac{\partial q_i}{\partial t} \Big|_{gr} = - \frac{\partial}{\partial p} \{ q_a \times \rho g V_f \times (q_i / q_a) \} \quad (\text{A6})$$

578 where V_f is the fall speed the cloud ice fall as relative to the large-scale vertical motion and is
 579 parameterized as:

$$V_f = 3.29(\rho q_i/q_a)^{0.16} \quad (\text{A7})$$

580 *b. Conversions between Liquid and Ice*

581 *BF Process*: the time rate change of the Bergeron-Findeisen process (growth of an ice crystal
 582 from preferential condensation) is parameterized as:

$$\left. \frac{\partial q_l}{\partial t} \right|_{\text{berg}} = - \frac{q_a \times (N_i/\rho)^{2/3} \times 7.8 \times (\text{MAX}(q_i/q_a, M_{i0}N_i/\rho))^{1/3}}{(\rho_i)^{2/3} \times (A + B)} \quad (\text{A8})$$

583 where N_i is the number of ice nuclei per unit volume, M_{i0} is the mass (10^{-12}) of an initial
 584 crystal assumed to always be present, ρ_i is the mass density of pristine ice crystals. Additionally,
 585 $A = (L_v/K_a T) \cdot ((L_v/R_v T) - 1)$ and $B = R_v T / \chi e_s$, where K_a is the thermal conductivity of air, χ
 586 is the diffusivity of water vapor in air, and R_v is the gas constant for water vapor. The ice nuclei
 587 density, N_i , is parameterized assuming the air is a liquid water saturation:

$$N_i = 1000 \exp \left[12.96 \frac{(e_{sl} - e_{si})}{e_{si}} - 0.639 \right] \quad (\text{A9})$$

588 where e_{sl} and e_{si} are the saturation vapor pressures over liquid and ice, respectively.

589 *Riming*: the time rate change of riming (falling ice colliding and coalescing with cloud droplets)
 590 is parameterized as:

$$\left. \frac{\partial q_l}{\partial t} \right|_{\text{rim}} = -a_{\text{snow}}^{\text{cld}} \times \lambda_f E_{c,\text{rim}} (R_{\text{snow}}^{\text{cld}} / 2\rho_i a_{\text{snow}}^{\text{cld}}) \times (q_l/q_a) \quad (\text{A10})$$

591 where ρ_i is the assumed density of falling ice crystals, $R_{\text{snow}}^{\text{cld}}$ is the grid mean flux of settling ice
 592 entering the rid box from above that enters saturated air, $a_{\text{snow}}^{\text{cld}}$ is the portion of the grid box that this
 593 occurs in, $E_{c,\text{rim}}$ is the collection efficiency for the riming process (fixed), and λ_f is parameterized
 594 as a function of temperature:

$$\lambda_f = 1.6 \times 10^3 \cdot 10^{0.023(276.16K - T)} \quad (\text{A11})$$

References

- Betts, A. K., and Harshvardhan, 1987: Thermodynamic constraint on the cloud liquid water feedback in climate models. *J. Geophys. Res.*, **92**, 8483–8485, doi:10.1029/JD092iD07p08483.
- Bjordal, J., T. Storelvmo, K. Alterskjær, and T. Carlsen, 2020: Equilibrium climate sensitivity above 5°C plausible due to state-dependent cloud feedback. *Nat. Geosci.*, **23**, 718–721, doi:10.1038/s41561-020-00649-1.
- Bodas-Salcedo, A., P. G. Hill, K. Furtado, K. D. Williams, P. R. Field, J. C. Manners, P. Hyder, and S. Kato, 2016: Large contribution of supercooled liquid clouds to the solar radiation budget of the Southern Ocean. *J. Climate*, **29**, 4213–4228, doi:10.1175/JCLI-D-15-0564.1.
- Bodas-Salcedo, A., J. P. Mulcahy, T. Andrews, K. D. Williams, M. A. Ringer, P. R. Field, and G. S. Elsaesser, 2019: Strong dependence of atmospheric feedbacks on mixed-phase microphysics and aerosol-cloud interactions in HadGEM3. *J. Adv. Model. Earth Syst.*, **11**, 1735–1758, doi:10.1029/2019MS001688.
- Ceppi, P., F. Brient, M. D. Zelinka, and D. L. Hartmann, 2017: Cloud feedback mechanisms and their representation in global climate models. *WIREs Clim. Change*, **8**, doi:10.1002/wcc.465.
- Ceppi, P., and D. L. Hartmann, 2015: Connections between clouds, radiation, and midlatitude dynamics: A review. *Curr. Clim. Change. Rep.*, **1**, 94–102, doi:10.1007/s40641-015-0010-x.
- Ceppi, P., D. L. Hartmann, and M. J. Webb, 2016: Mechanisms of the negative shortwave cloud feedback in middle to high latitudes. *J. Climate*, **29**, 139–157, doi:10.1175/JCLI-D-15-0327.1.
- Cesana, G., and T. Storelvmo, 2017: Improving climate projections by understanding how cloud phase affects radiation. *J. Geophys. Res. Atmos.*, **122**, 4594–4599, doi:10.1002/2017JD026927.

616 Cesana, G., D. E. Waliser, X. Jiang, and J. F. Li, 2015: Multimodel evaluation of cloud phase
617 transition using satellite and reanalysis data. *J. Geophys. Res. Atmos.*, **120**, 7871–7892, doi:
618 10.1002/2014JD022932.

619 Frey, W. R., and J. E. Kay, 2018: The influence of extratropical cloud phase and amount feedbacks
620 on climate sensitivity. *Climate Dyn.*, **50**, 3097–3116, doi:10.1007/s00382-017-3796-5.

621 Galewsky, J., A. Sobel, and I. M. Held, 2005: Diagnosis of subtropical humidity dynamics using
622 tracers of last saturation. *J. Atmos. Sci.*, **62**, 3353–3367, doi:10.1175/JAS3533.1.

623 Gettelman, A., and S. C. Sherwood, 2016: Processes responsible for cloud feedback. *Curr. Clim.*
624 *Change Rep.*, **2**, 179–189, doi:10.1007/s40641-016-0052-8.

625 Golaz, J. C., M. Salzmann, L. J. Donner, L. W. Horowitz, Y. Ming, and M. Zhao, 2011:
626 Sensitivity of the aerosol indirect effect to subgrid variability in the cloud parameterization
627 of the GFDL atmosphere general circulation model AM3. *J. Climate*, **24**, 3145–3160, doi:
628 10.1175/2010JCLI3945.1.

629 Gordon, N. D., and S. A. Klein, 2014: Low-cloud optical depth feedback in climate models. *J.*
630 *Geophys. Res. Atmos.*, **119**, 6052–6065, doi:10.1002/2013JD021052.

631 Held, I. M., 2005: The gap between simulation and understanding in climate modeling. *Bull. Amer.*
632 *Meteor. Soc.*, **86**, 1609–1614, doi:10.1175/BAMS-86-11-1609.

633 Held, I. M., 2014: Simplicity amid complexity. *Science*, **343**, 1206–1207, doi:10.1126/science.
634 1248447.

635 Held, I. M., and M. J. Suarez, 1994: A proposal for the intercomparison of the dynamical
636 cores of atmospheric general circulation models. *Bull. Amer. Meteor. Soc.*, **75**, 1825–1830,
637 doi:10.1175/1520-0477(1994)075<1825:APFTIO>2.0.CO;2.

638 Kanji, Z. A., L. A. Ladino, H. Wex, Y. Boose, M. Burkert-Kohn, D. J. Cziczo, and
639 M. Krämer, 2017: Overview of ice nucleating particles. *Meteor. Monogr.*, **58**, 1.1–1.33, doi:
640 10.1175/AMSMONOGRAPHS-D-16-0006.1.

641 Kay, J. E., B. Medeiros, Y.-T. Hwang, A. Gettelman, J. Perket, and M. G. Flanner, 2014: Processes
642 controlling Southern Ocean shortwave climate feedbacks in CESM. *Geophys. Res. Lett.*, **41**,
643 616–622, doi:10.1002/2013GL058315.

644 Klein, S. A., and Coauthors, 2009: Intercomparison of model simulations of mixed-phase clouds
645 observed during the ARM Mixed-Phase Arctic Cloud Experiment. I: Single-layer cloud. *Quart.*
646 *J. Roy. Meteor. Soc.*, **135**, 979–1002, doi:10.1002/qj.416.

647 Korolev, A., and Coauthors, 2017: Mixed-phase clouds: Progress and challenges. *Meteor. Monogr.*,
648 **58**, 5.1–5.50, doi:10.1175/AMSMONOGRAPHS-D-17-0001.1.

649 Lohmann, U., and D. Neubauer, 2018: The importance of mixed-phase and ice clouds for climate
650 sensitivity in the global aerosol–climate model ECHAM6-HAM2. *Atmos. Chem. Phys.*, **18**,
651 8807–8828, doi:10.5194/acp-18-8807-2018.

652 Lohmann, U., and E. Roeckner, 1996: Design and performance of a new cloud microphysics
653 scheme developed for the ECHAM general circulation model. *Climate Dyn.*, **12**, 557–572,
654 doi:10.1007/BF00207939.

655 McCoy, D. T., P. Field, A. Bodas-Salcedo, G. S. Elsaesser, and M. D. Zelinka, 2020: A regime-
656 oriented approach to observationally constraining extratropical shortwave cloud feedbacks. *J.*
657 *Climate*, **33**, 9967–9983, doi:10.1175/JCLI-D-19-0987.1.

- 658 McCoy, D. T., D. L. Hartmann, and D. P. Grosvenor, 2014: Observed Southern Ocean cloud prop-
659 erties and shortwave reflection. Part I: Calculation of SW flux from observed cloud properties.
660 *J. Climate*, **27**, 8836–8857, doi:10.1175/JCLI-D-14-00287.1.
- 661 McCoy, D. T., D. L. Hartmann, and M. D. Zelinka, 2018: Mixed-phase cloud feedbacks. *Mixed-*
662 *Phase Clouds: Observations and Modeling*, C. Andronache, Ed., Elsevier, 215–236, doi:10.
663 1016/B978-0-12-810549-8.00009-X.
- 664 McCoy, D. T., D. L. Hartmann, M. D. Zelinka, P. Ceppi, and D. P. Grosvenor, 2015: Mixed-phase
665 cloud physics and Southern Ocean cloud feedback in climate models. *J. Geophys. Res. Atmos.*,
666 **120**, 9539–9554, doi:10.1002/2015JD023603.
- 667 McCoy, D. T., I. Tan, D. L. Hartmann, M. D. Zelinka, and T. Storelvmo, 2016: On the relationships
668 among cloud cover, mixed-phase partitioning, and planetary albedo in GCMs. *J. Adv. Model.*
669 *Earth Syst.*, **8**, 650–668, doi:10.1002/2015MS000589.
- 670 McCoy, D. T., and Coauthors, 2019: Cloud feedbacks in extratropical cyclones: insight from long-
671 term satellite data and high-resolution global simulations. *Atmos. Chem. Phys.*, **19**, 1147–1172,
672 doi:10.5194/acp-19-1147-2019.
- 673 McCoy, D. T., and Coauthors, 2021: Extratropical shortwave cloud feedbacks in the context of the
674 global circulation and hydrological cycle. *under review in GRL*.
- 675 Ming, Y., and I. M. Held, 2018: Modeling water vapor and clouds as passive tracers in an idealized
676 GCM. *J. Climate*, **31**, 775–786, doi:10.1175/JCLI-D-16-0812.1.
- 677 Mitchell, J., C. Senior, and W. Ingram, 1989: CO₂ and climate: a missing feedback? *Nature*, **341**,
678 132–134, doi:10.1038/341132a0.

- 679 Morrison, H., and A. Gettelman, 2008: A new two-moment bulk stratiform cloud microphysics
680 scheme in the Community Atmosphere Model, version 3 (CAM3). Part I: Description and
681 numerical tests. *J. Climate*, **21**, 3642–3659, doi:10.1175/2008JCLI2105.1.
- 682 Mülmenstädt, J., and Coauthors, 2021: An underestimated negative cloud feedback from cloud
683 lifetime changes. *Nat. Clim. Change*, **11**, 508–513, doi:10.1038/s41558-021-01038-1.
- 684 Pierrehumbert, R. T., H. Brogniez, and R. Roca, 2007: On the relative humidity of the atmosphere.
685 *The Global Circulation of the Atmosphere*, T. Schneider, and A. H. Sobel, Eds., Princeton
686 University Press, 143–185.
- 687 Pruppacher, H., and J. Klett, 2010: Cloud chemistry. *Microphysics of Clouds and Precipitation*,
688 *Atmospheric and Oceanographic Sciences Library, vol. 18*, Springer, 237–264, doi:10.1007/
689 978-0-306-48100-0_17.
- 690 Rotstajn, L. D., 1997: A physically based scheme for the treatment of stratiform clouds and
691 precipitation in large-scale models. I: Description and evaluation of the microphysical processes.
692 *Q. J. R. Meteorol. Soc.*, **123**, 1227–1282.
- 693 Rotstajn, L. D., B. F. Ryan, and J. J. Katzfey, 2000: A scheme for calculation of the liquid fraction
694 in mixed-phase clouds in large-scale models. *Mon. Wea. Rev.*, **128**, 1070–1088.
- 695 Senior, C. A., and J. F. B. Mitchell, 1993: Carbon dioxide and climate: The impact of cloud
696 parameterization. *J. Climate*, **6**, 393–418, doi:10.1175/1520-0442(1993)006<0393:CDACTI>
697 2.0.CO;2.
- 698 Sherwood, S. C., and Coauthors, 2020: An assessment of Earth’s climate sensitivity using multiple
699 lines of evidence. *Reviews of Geophysics*, **58**, e2019RG000678, doi:10.1029/2019RG000678.

700 Soden, B. J., and G. A. Vecchi, 2011: The vertical distribution of cloud feedback in coupled
701 ocean-atmosphere models. *Geophys. Res. Lett.*, **38**, L12 704, doi:10.1029/2011GL047632.

702 Somerville, R. C. J., and L. A. Remer, 1984: Cloud optical thickness feedbacks in the CO₂ climate
703 problems. *J. Geophys. Res. Atmos.*, **89**, 9668–9672, doi:10.1029/JD089iD06p09668.

704 Stephens, G. L., 1978: Radiation profiles in extended water clouds. II. Parameterization schemes.
705 *J. Atmos. Sci.*, **35**, 2123–2132, doi:10.1175/1520-0469(1978)035<2123:RPIEWC>2.0.CO;2.

706 Storelvmo, T., I. Tan, and A. V. Korolev, 2015: Cloud phase changes induced by CO₂ warming—a
707 powerful yet poorly constrained cloud-climate feedback. *Curr. Clim. Change Rep.*, **1**, 288–296,
708 doi:10.1007/s40641-015-0026-2.

709 Tan, I., L. Oreopoulos, and N. Cho, 2019: The role of thermodynamic phase shifts in cloud
710 optical depth variations with temperature. *Geophys. Res. Lett.*, **46**, 4502–4511, doi:10.1029/
711 2018GL081590.

712 Tan, I., and T. Storelvmo, 2016: Sensitivity study on the influence of cloud microphysical pa-
713 rameters on mixed-phase cloud thermodynamic phase partitioning in CAM5. *J. Atmos. Sci.*, **73**,
714 709–728, doi:10.1175/JAS-D-15-0152.1.

715 Tan, I., and T. Storelvmo, 2019: Evidence of strong contributions from mixed-phase clouds to
716 Arctic climate change. *Geophys. Res. Lett.*, **46**, 2894–2902, doi:10.1029/2018GL081871.

717 Tan, I., T. Storelvmo, and M. D. Zelinka, 2016: Observational constraints on mixed-phase clouds
718 imply higher climate sensitivity. *Science*, **352**, 224–227, doi:10.1126/science.aad5300.

719 Tan, I., T. Storelvmo, and M. D. Zelinka, 2018: The climatic impact of thermodynamic phase
720 partitioning in mixed-phase clouds. *Mixed-Phase Clouds: Observations and Modeling*, C. An-
721 dronache, Ed., Elsevier, 237–264, doi:10.1016/B978-0-12-810549-8.00010-6.

722 Terai, C., R. Y. Zhang, S. A. Klein, M. D. Zelinka, J. C. Chiu, and Q. Min, 2019: Mechanisms
723 behind the extratropical stratiform low-cloud optical depth response to temperature in ARM site
724 observations. *J. Geophys. Res. Atmos.*, **124**, 2127–2147, doi:10.1029/2018JD029359.

725 Terai, C. R., S. A. Klein, and M. D. Zelinka, 2016: Constraining the low-cloud optical depth
726 feedback at middle and high latitudes using satellite observations. *J. Geophys. Res. Atmos.*, **121**,
727 9696–9716, doi:10.1002/2016JD025233.

728 Tselioudis, G. W., B. Rossow, and D. Rind, 1992: Global patterns of cloud optical thickness
729 variation with temperature. *J. Climate*, **5**, doi:0.1175/1520-0442(1992)005<1484:GPOCOT>2.
730 0.CO;2.

731 Vial, J., J.-L. Dufresne, and S. Bony, 2013: On the interpretation of inter-model spread in CMIP5
732 climate sensitivity estimates. *Climate Dyn.*, **41**, 3339–3362, doi:10.1007/s00382-013-1725-9.

733 Wall, C. J., and D. L. Hartmann, 2015: On the influence of poleward jet shift on shortwave cloud
734 feedback in global climate models. *J. Adv. Model. Earth Syst.*, **7**, doi:10.1002/2015MS000520.

735 Zelinka, M. D., T. A. Myers, D. T. McCoy, S. Po-Chedley, P. M. Caldwell, P. Ceppi, S. A. Klein,
736 and K. E. Taylor, 2020: Causes of higher climate sensitivity in CMIP6 models. *Geophys. Res.*
737 *Lett.*, **47**, e2019GL085782, doi:10.1029/2019GL085782.

738 Zelinka, M. D., C. Zhou, and S. A. Klein, 2016: Insights from a refined decomposition of cloud
739 feedbacks. *Geophys. Res. Lett.*, **43**, 9259–9269, doi:10.1002/2016GL069917.

740 Zhao, M., 2014: An investigation of the connections among convection, clouds, and climate
741 sensitivity in a global climate model. *J. Climate*, **27**, 1845–1862, doi:10.1175/JCLI-D-13-00145.
742 1.

743 **LIST OF TABLES**

744 **Table 1.** Description of the experiments. 36

745 **Table 2.** Normalized changes in LWP and IWP ($\text{g m}^{-2} \text{K}^{-1}$) in the process-level exper-
746 iments. The normalized fractional changes ($\% \text{K}^{-1}$) are in parentheses. The
747 climatological values (g m^{-2}) in Ctrl are also given. 37

TABLE 1. Description of the experiments.

Name(s)	Perturbation(s)
Ctrl	the control with $RH_c = 83.3\%$
Tse2K	2-K warming applied to the temperature seen by the (stratiform) cloud scheme and surface evaporation
Process-level Experiments (Section 3a)	
Qse2K	2-K warming applied to calculation of q_s for the cloud scheme and surface evaporation
MI2K	2-K warming applied to <i>microphysical</i> processes: BF process, melting, homogeneous freezing, and initial phase partitioning
BF2K	2-K warming applied to the <i>BF</i> process
ME2K	2-K warming applied to <i>melting</i>
Perturbed Parameter Experiments (Section 3b)	
{quar, halv, doub, quad}BF	the BF conversion rate multiplied by {0.25, 0.5, 2, 4}
rh{767, 800, 867, 900}	$RH_c = \{76.7\%, 80\%, 86.7\%, 90\%\}$
v{050, 075, 125, 150}	the ice fall speed multiplied by {0.5, 0.75, 1.25, 1.5}
{name}_Tse2K	the corresponding Tse2K experiment for {name} (e.g., quarBF_Tse2K)

748 TABLE 2. Normalized changes in LWP and IWP ($\text{g m}^{-2} \text{K}^{-1}$) in the process-level experiments. The normalized
 749 fractional changes ($\% \text{K}^{-1}$) are in parentheses. The climatological values (g m^{-2}) in Ctrl are also given.

	Extratropics		Mid-Latitudes		High-Latitudes	
	LWP	IWP	LWP	IWP	LWP	IWP
Ctrl	29.9	35.6	38.3	42.7	4.6	14.1
Tse2K	3.0 (9.9)	0.9 (2.4)	3.6 (9.3)	0.8 (1.9)	1.1 (24.2)	1.0 (7.2)
Qse2K	0.5 (1.7)	2.4 (6.8)	0.6 (1.6)	2.8 (6.7)	0.2 (5.2)	1.1 (7.9)
MI2K	2.2 (7.4)	-1.4 (-4.0)	2.6 (6.9)	-1.9 (-4.4)	0.9 (19.4)	0.0 (-0.3)
BF2K	1.7 (5.5)	-0.1 (-0.2)	1.9 (5.0)	-0.1 (-0.2)	0.9 (18.7)	0.0 (0.2)
ME2K	0.6 (2.1)	-1.4 (-3.9)	0.8 (2.1)	-1.8 (-4.2)	0.0 (0.8)	-0.1 (-0.5)

LIST OF FIGURES

750

751 **Fig. 1.** Schematic of tracers and processes in the cloud microphysics scheme. Quantities in rectangles are prognostic tracers, and those in ovals are diagnostic variables. 39

752

753 **Fig. 2.** Zonal-mean LWP and IWP (g m^{-2}) in Ctrl and Tse2K experiments, averaged between

754 hemispheres as for all following figures. 40

755 **Fig. 3.** Normalized changes in the zonal-mean extratropical LWP (the upper panels) and IWP (the

756 lower panels) ($\text{g m}^{-2} \text{K}^{-1}$) in the process-level experiments. 41

757 **Fig. 4.** Vertical distributions of the normalized changes in the zonal-mean mixing ratios of cloud

758 liquid and ice ($10^{-6} \text{kg kg}^{-1} \text{K}^{-1}$) in the key process-level experiments. Differences between

759 the perturbation and Ctrl runs are shown as colored shading. Ctrl run values are depicted by

760 the contours with a spacing of $5 \cdot 10^{-6} \text{kg kg}^{-1}$. Thick grey lines show the 0°C and -40°C

761 isotherms. The x- and y-axes are latitude and pressure (hPa), respectively. 42

762 **Fig. 5.** Vertical distributions of the normalized changes in the zonal-mean time tendency terms

763 of cloud liquid mixing ratio ($10^{-9} \text{kg kg}^{-1} \text{s}^{-1} \text{K}^{-1}$) in the key process-level experiments.

764 Differences between the perturbation and Ctrl runs are shown as colored shading where a

765 positive value indicates an increase in cloud liquid tendency. Ctrl run values are represented

766 by the contours with a spacing of $1 \cdot 10^{-9} \text{kg kg}^{-1} \text{s}^{-1}$. The tendency terms shown are

767 condensation, autoconversion, accretion, the BF process, and riming. Thick grey lines are

768 the 0°C and -40°C isotherms. The x- and y-axes are latitude and pressure (hPa), respectively. 43

769 **Fig. 6.** As Fig. 5, but for cloud ice instead of cloud liquid, with tendency terms shown being the BF

770 process, riming, and gravitational ice settling. 44

771 **Fig. 7.** Summary of the three main processes (highlighted by Qse2K, BF2K, and ME2K experi-

772 ments) underlying the LWP/IWP feedback. Arrow width and direction represent the relative

773 magnitude and sign (upward denoting an increase) of the extratropical LWP/IWP changes,

774 respectively. 45

775 **Fig. 8.** Climatological extratropical LWP (g m^{-2}) plotted against the climatological extratropical

776 IWP (g m^{-2}) in the perturbed parameter experiments. 46

777 **Fig. 9.** Normalized changes in extratropical LWP/IWP ($\text{g m}^{-2} \text{K}^{-1}$) in the full warming (Tse2K) ex-

778 periments plotted against the climatological extratropical LWP/IWP (g m^{-2}) in the perturbed

779 parameter experiments. Panels (a) and (b) are for LWP and IWP, respectively. The rectangle

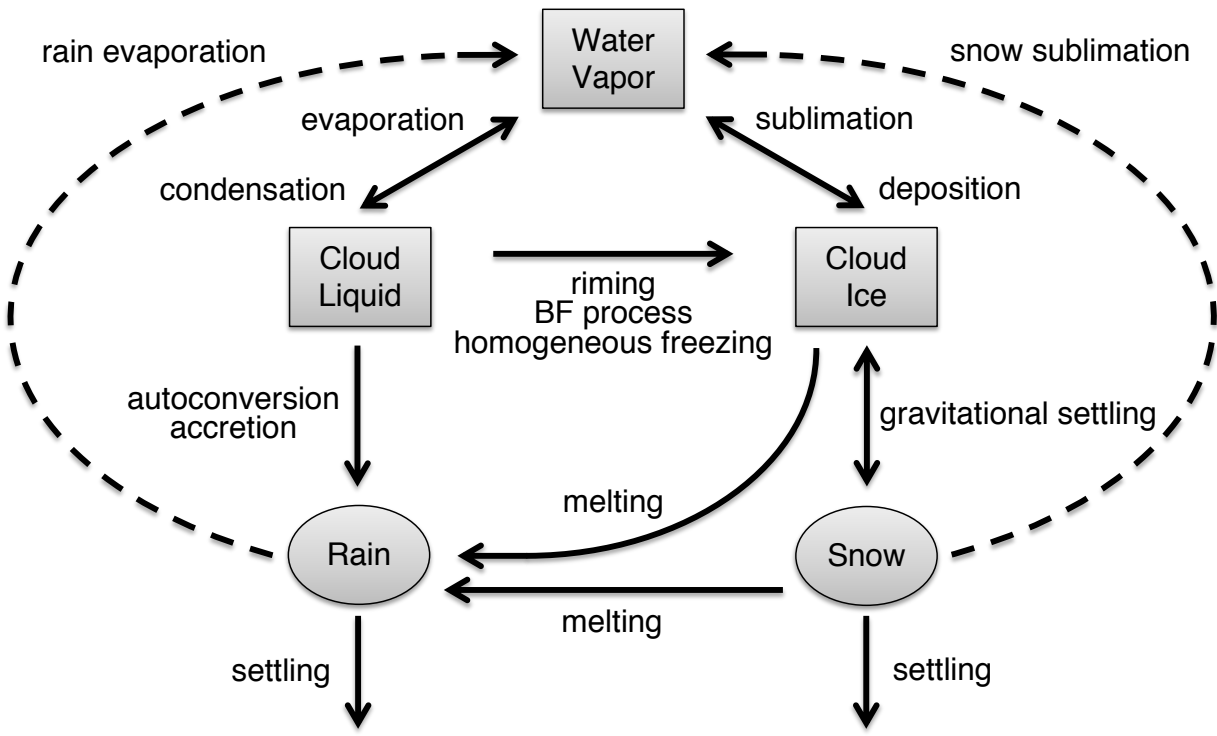
780 in Panel (b) is a blowup of the data points clustered around Ctrl. 47

781 **Fig. 10.** Normalized changes in extratropical LWP ($\text{g m}^{-2} \text{K}^{-1}$) in the full warming (Tse2K) ex-

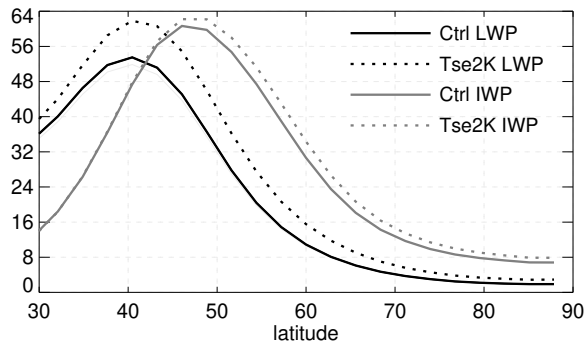
782 periments plotted against the climatological extratropical T5050 in the perturbed parameter

783 experiments. The black and orange dotted lines represent the best linear fits without and

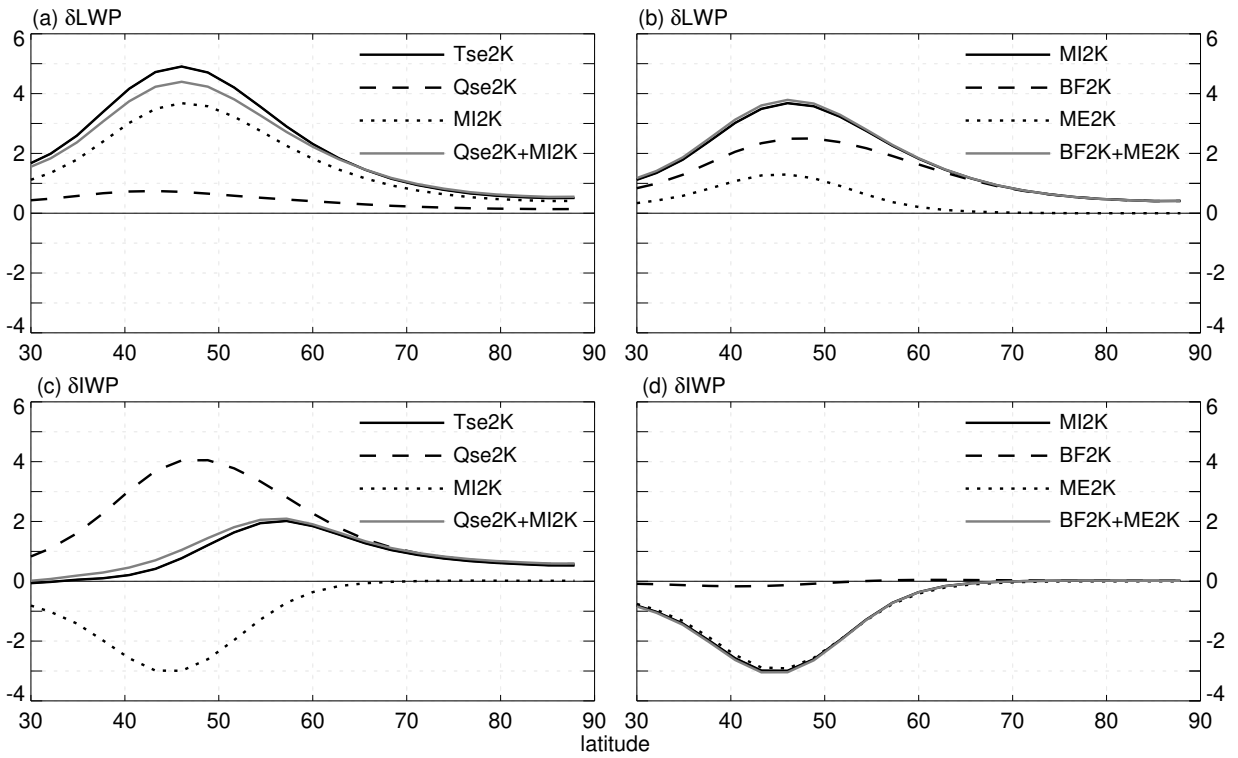
784 with the ice fall speed experiments, respectively. 48



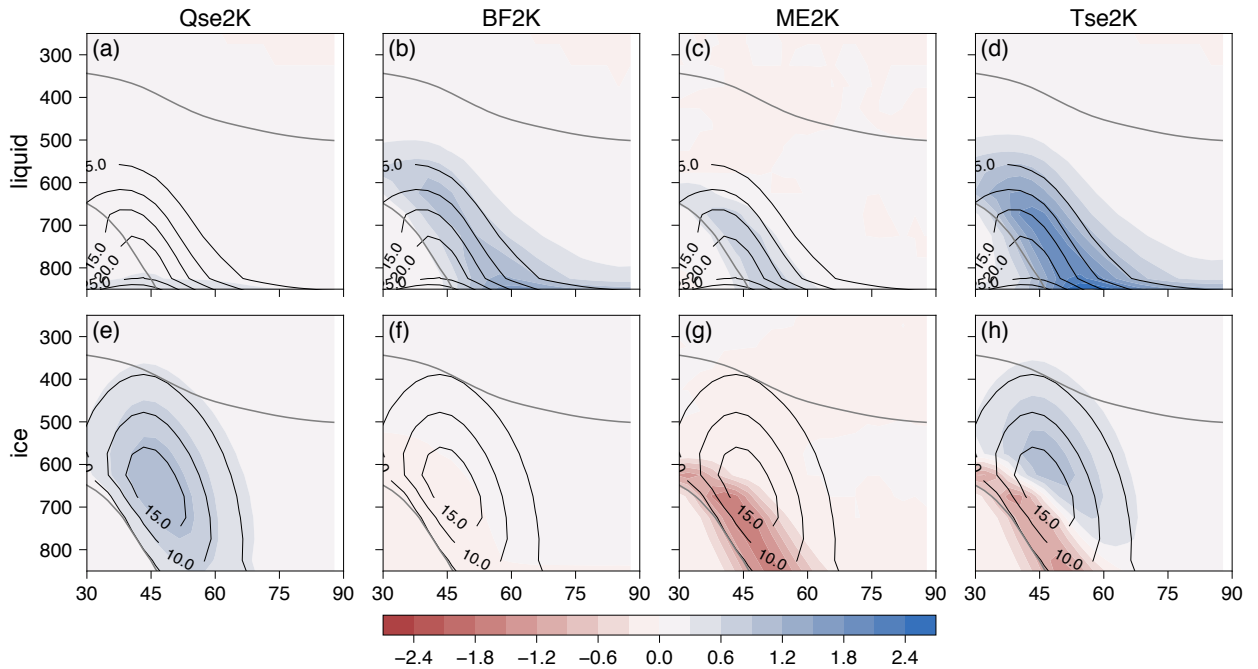
785 FIG. 1. Schematic of tracers and processes in the cloud microphysics scheme. Quantities in rectangles are
 786 prognostic tracers, and those in ovals are diagnostic variables.



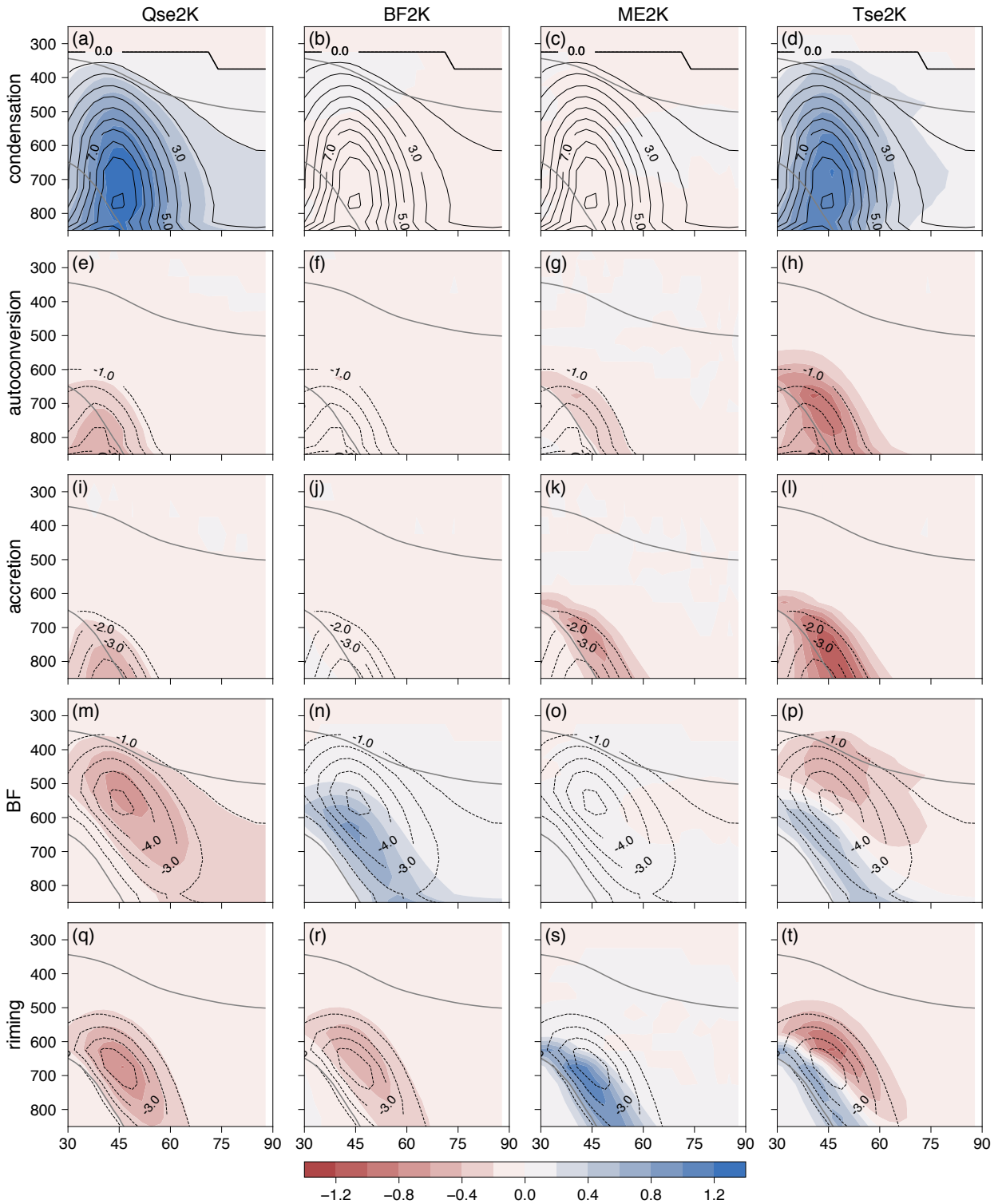
787 FIG. 2. Zonal-mean LWP and IWP (g m^{-2}) in Ctrl and Tse2K experiments, averaged between hemispheres as
 788 for all following figures.



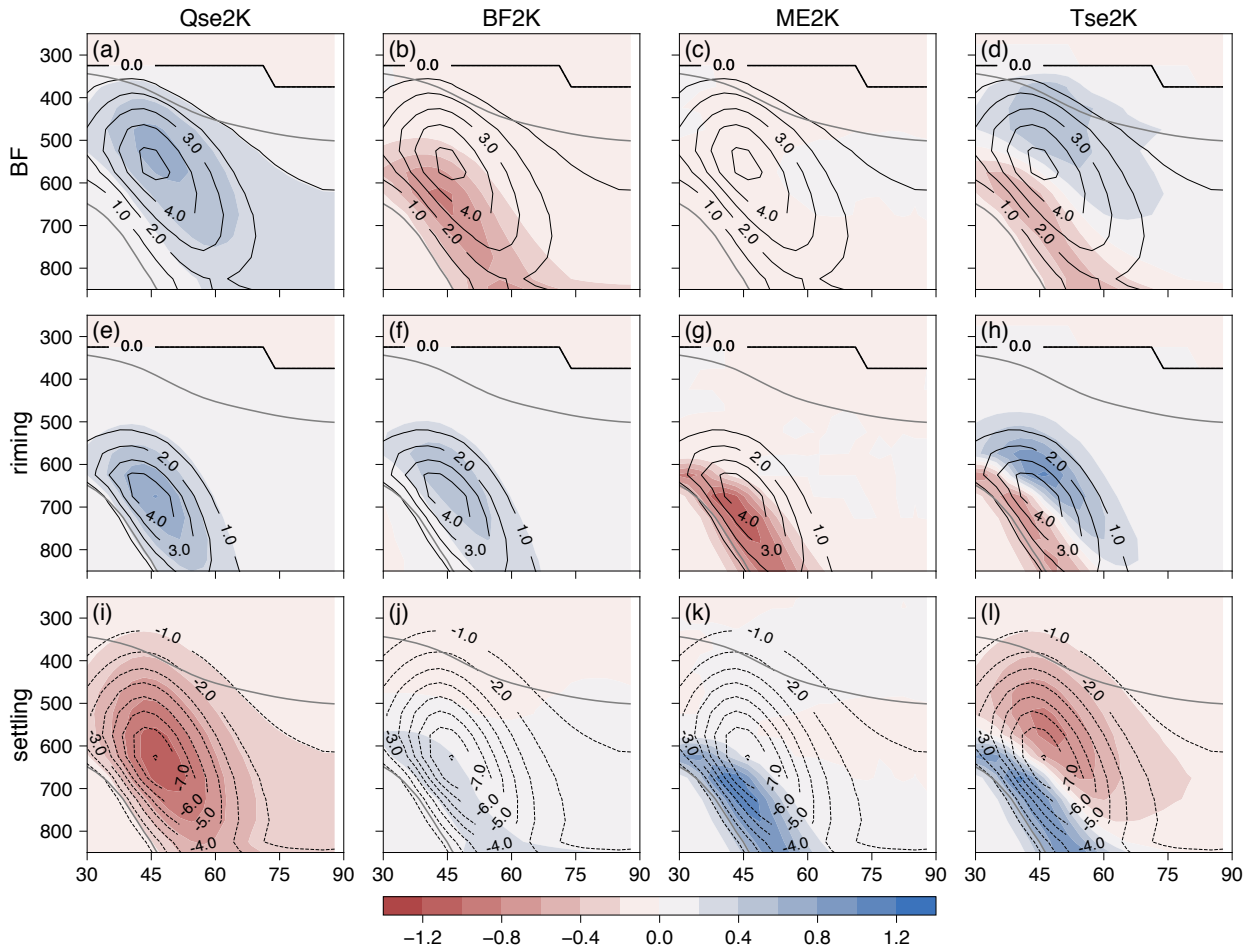
789 FIG. 3. Normalized changes in the zonal-mean extratropical LWP (the upper panels) and IWP (the lower
790 panels) ($\text{g m}^{-2} \text{K}^{-1}$) in the process-level experiments.



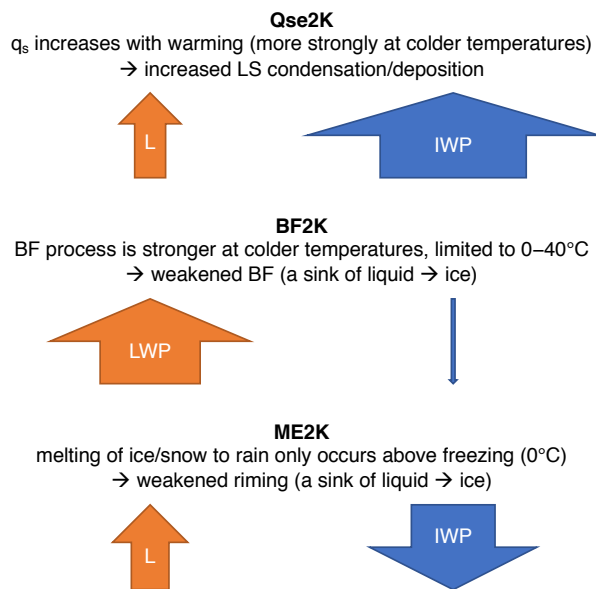
791 FIG. 4. Vertical distributions of the normalized changes in the zonal-mean mixing ratios of cloud liquid and ice
 792 ($10^{-6} \text{ kg kg}^{-1} \text{ K}^{-1}$) in the key process-level experiments. Differences between the perturbation and Ctrl runs are
 793 shown as colored shading. Ctrl run values are depicted by the contours with a spacing of $5 \cdot 10^{-6} \text{ kg kg}^{-1}$. Thick
 794 grey lines show the 0°C and -40°C isotherms. The x- and y-axes are latitude and pressure (hPa), respectively.



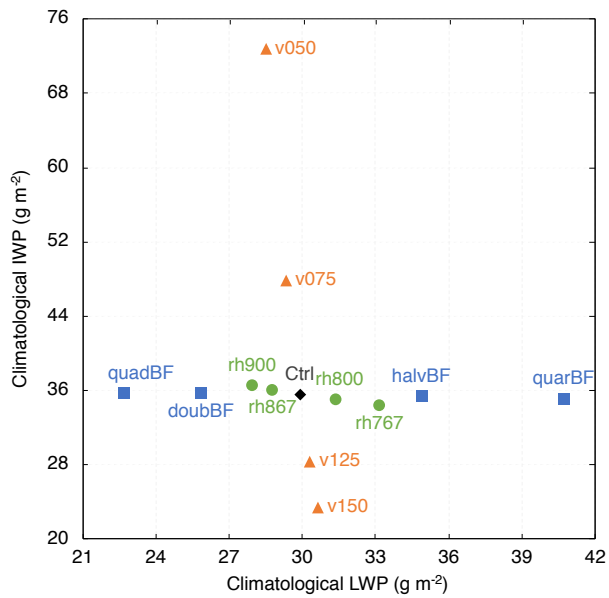
795 FIG. 5. Vertical distributions of the normalized changes in the zonal-mean time tendency terms of cloud liquid
 796 mixing ratio ($10^{-9} \text{ kg kg}^{-1} \text{ s}^{-1} \text{ K}^{-1}$) in the key process-level experiments. Differences between the perturbation
 797 and Ctrl runs are shown as colored shading where a positive value indicates an increase in cloud liquid tendency.
 798 Ctrl run values are represented by the contours with a spacing of $1 \cdot 10^{-9} \text{ kg kg}^{-1} \text{ s}^{-1}$. The tendency terms shown
 799 are condensation, autoconversion, accretion, the BF process, and riming. Thick grey lines are the 0°C and -40°C



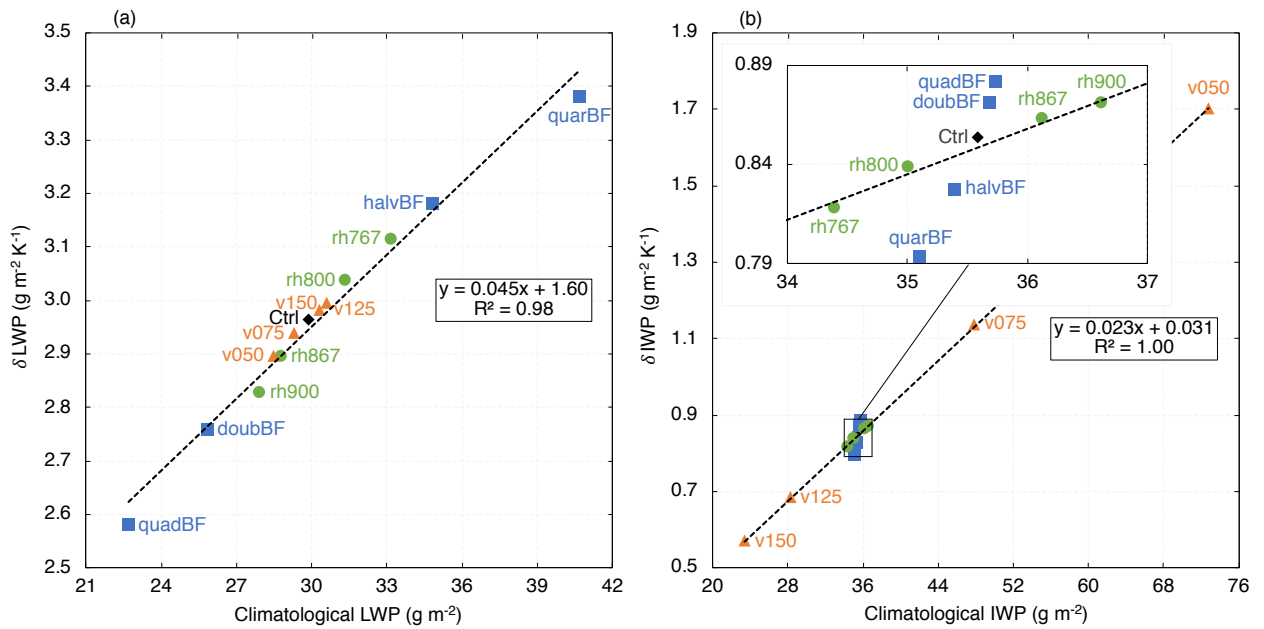
801 FIG. 6. As Fig. 5, but for cloud ice instead of cloud liquid, with tendency terms shown being the BF process,
 802 riming, and gravitational ice settling.



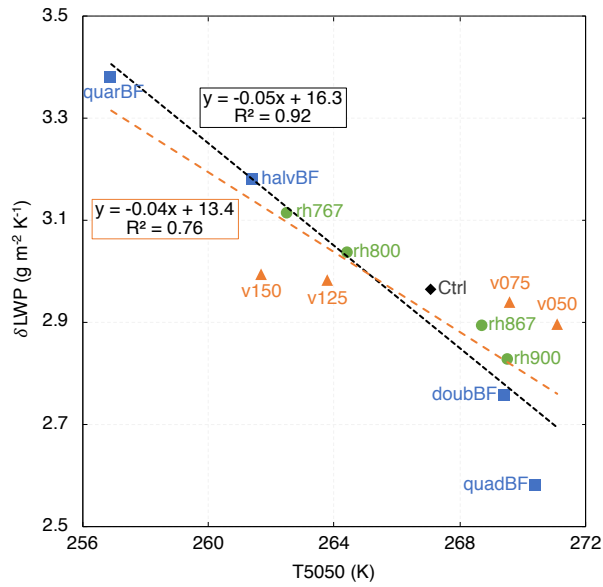
803 FIG. 7. Summary of the three main processes (highlighted by Qse2K, BF2K, and ME2K experiments)
 804 underlying the LWP/IWP feedback. Arrow width and direction represent the relative magnitude and sign
 805 (upward denoting an increase) of the extratropical LWP/IWP changes, respectively.



806 FIG. 8. Climatological extratropical LWP (g m^{-2}) plotted against the climatological extratropical IWP (g m^{-2})
 807 in the perturbed parameter experiments.



808 FIG. 9. Normalized changes in extratropical LWP/IWP ($\text{g m}^{-2} \text{K}^{-1}$) in the full warming (Tse2K) experiments
 809 plotted against the climatological extratropical LWP/IWP (g m^{-2}) in the perturbed parameter experiments. Panels
 810 (a) and (b) are for LWP and IWP, respectively. The rectangle in Panel (b) is a blowup of the data points clustered
 811 around Ctrl.



812 FIG. 10. Normalized changes in extratropical LWP ($\text{g m}^{-2} \text{K}^{-1}$) in the full warming (Tse2K) experiments
 813 plotted against the climatological extratropical T5050 in the perturbed parameter experiments. The black and
 814 orange dotted lines represent the best linear fits without and with the ice fall speed experiments, respectively.